Complex, evolving patterns of mass loss from Antarctica's largest glacier

Jonathan L. Bamber[1*], Geoffrey Dawson[1]

[1]Bristol Glaciology Centre, University of Bristol, Bristol, UK

*Correspondence to: j.bamber@bristol.ac.uk

Pine Island Glacier has contributed more to sea level rise over the last four decades than any other glacier in Antarctica. Model projections indicate that this will continue in the future but at conflicting rates. Some models suggest that mass loss could dramatically increase over the next few decades, resulting in a rapidly growing contribution to sea level, and fast retreat of the grounding line, where the grounded ice meets the ocean. Other models indicate more moderate losses. Resolving this contrasting behaviour is important for sea level rise projections. Here, we use high resolution satellite observations of elevation change since 2010 to show that thinning rates are now highest along the slow-flow margins of the glacier and that the present-day amplitude and pattern of elevation change is inconsistent with fast grounding line migration and the associated rapid increase in mass loss over the next few decades. Instead, our results support model simulations that imply only modest changes in grounding line location over that timescale. We demonstrate how the pattern of thinning is evolving in complex ways both in space and time and how rates in the fast-flowing central trunk have decreased by about a factor five since 2007.

Pine Island Glacier (PIG) has been the single largest contributor to sea level rise from the continent [1]. Combined with its neighbour, Thwaites Glacier, it contributes 32% of the ice discharge from the West Antarctic Ice Sheet (WAIS). This region, the Amundsen Sea

Embayment (ASE), has been described as the "weak underbelly" of the WAIS because of the steep retrograde bedrock slope that it rests on which reaches up to 2500 m below sea level in the interior [2]. As a consequence of its recent behaviour and its inferred importance for the stability of the WAIS, PIG is one of the most intensively and extensively investigated glacier system in Antarctica, including numerous satellite [3-5], modelling [6-9] and field studies [10-12] aimed at understanding its response to external forcing, the geophysical controls on mass loss and, in turn, improving projections of its future trends.

Recent behaviour and model projections

Sustained retreat of the grounding line and linearly increasing thinning rate at the hinge-line has been reported between 1992 and 2011, with thinning rates exceeding 7 m/yr in 2007-2008 near the grounding line [13]. The grounding-line retreat coincided with an inland migration of surface lowering, which was confined to the central trunk up to 2004 [5,14]. From 2004 onward, thinning spread inland with the maximum rates appearing to be concentrated in regions of faster flow and approximately following the velocity contours into the glacier tributaries [5,15]. Numerical modelling suggested that this could be explained by a diffusive process resulting from reduced basal friction at the grounding line that could be transmitted about 200 km inland over a decadal time scale [16]. More recently, a study using three different numerical ice sheet models, concluded that the grounding line had started an irreversible retreat that could result in a major increase in ice discharge over the next few decades [9]. For a plausible melt scenario, they found that the mass imbalance could increase by as much as a factor six, resulting in an additional sea level contribution of up to 10 mm in the next 20 years [9]. This is, however, at odds with other studies that suggest that doubling [8] or quadrupling [6] sub-shelf basal melt rates will only have a modest impact on the projected sea level contribution. In the latter case, the 4 x melt experiment resulted

in an additional mass loss stabilising at 25 Gt/yr (1.4 mm sea level equivalent over 20 years). While these modelling studies agree that the glacier will remain out of balance, they produce markedly different trajectories into the future.

Observations of change since 2010

Volume change estimates of the PIG catchment have been based, until recently, on the analysis of satellite radar altimeter data using radar returns from the Point Of Closest Approach (POCA) to the satellite. Until the launch of CryoSat-2 in 2010, this was the only approach available for processing such data. It is, however, limited in the spatial resolution and sampling that can be achieved. Previous studies have gridded the data somewhere between 10 and 20 km, depending on the time interval and latitude. In addition, POCA data are biased in how they sample undulating terrain that is typical of the margins of the ice sheets [17]. The radar returns tend to be clustered around topographic highs and absent from troughs. CryoSat-2 has a unique capability known as the Synthetic Aperture Interferometric mode, which operates around the steeper, sloping margins of the Greenland and Antarctic ice sheets [18]. In addition to "conventional" POCA processing of the radar waveforms, the phase information recorded in this mode makes it possible to retrieve elevation estimates beyond the POCA location in the waveform [19]. This is known as swath processing and results in about two orders of magnitude greater sampling of the surface compared to POCA processing, but with data of lower accuracy and a dependency on knowledge of the satellite roll angle[19]. More importantly, swath data overcome the spatial sampling issues that POCA data can suffer from (Extended Fig 1). Combined with the long repeat cycle of CroySat-2 (369 days), dense radar altimeter sampling of the ice sheet margins is, for the first time, achievable. The approach has been successfully used to derive high resolution elevation change estimates from, for example, the Patagonian icefields [20]. Here, we use the

complete CryoSat-2 record from 2010-2018 to derive high resolution (500 m) elevation change estimates over PIG. We also investigate how the spatial pattern of elevation change has evolved over time.

Elevation rates for CryoSat-2 swath data were based on L1b baseline C data, processed using established methods [19]. To make optimal use of the high spatial sampling we mapped surface elevation rates on a grid of 500 m posting. This approach reduced the effect of topographic variability within a grid cell and allowed us to calculate a linear surface elevation rate at each grid cell (see Methods for further details). We calculated the time-mean surface elevation rate over the entire CryoSat-2 recorded from October 2010-2018 at 500 m posting (Figure 1) and for two periods between 2010-2014 and 2015-2018, with 2 km postings (Figure 2) as well as annually-resolved at a lower resolution (Extended Fig 2) to illustrate the evolution of the pattern of thinning. Mean surface elevation rates derived from ICESat-1 laser altimeter data (GLAS/ICESat L2 Global Land Surface Altimetry Data, version 34, GLA14) were also calculated using recent data pre-processing and repeat-track methods [21].

We also examined changes in velocity over the same time period. We used annual ice velocity maps from the MEaSUREs Version 1 data set [22] for the years 2005-2017 to calculate the velocity difference between the ICESat-1 and CryoSat-2 epochs. The GoLIVE velocity time series, recorded between 2013-2017 [23], was used to determine velocity change over the CryoSat-2 time period (for further information see Methods).

Mass loss from the PIG has been steadily increasing up until about 2009 and has dominated the contribution to sea level rise from the Antarctic Ice Sheet over the last decade [1,24]. This mass loss is associated with a speed-up of the glacier[1] and, based on the principle of conservation of mass, a concomitant reduction in volume (surface thinning). Ice speed remained relatively constant

92 from 2009-2014 (fluctuating by about 4 percent)[24], while , thinning rates peaked around 2008
93 [13,14]. Mass loss and the associated volume reduction, after this date, was sustained by inland
94 propagation of thinning rather than an increase in its amplitude.[7,24]. In Fig. 1, we compare
95 thinning rates derived from ICESat-1 for 2003-2009, with swath processed CryoSat-2 data from
96 2010-2018. For the earlier epoch, highest thinning rates are found in the central trunk of the
97 glacier, near the grounding line, consistent with previous assessments [5,14]. Up until about 2009,
98 the pattern of inland propagation is consistent with a diffusive process travelling upstream in
99 response to a transient forcing at the grounding line [14,16]. During the CryoSat 2 period, however,
100 the pattern of thinning is markedly different and reduced in amplitude, which is also supported
101 by a recent study employing digital elevation models derived from Worldview image stereo pairs
102 [13]. Changes in driving stress, due to a steeper slope at the glacier margin could be responsible for
103 the ice drawdown on the northern flank. We investigated this possibility by calculating the
104 change in slope and driving stress between Envisat, ICESat-1 and CryoSat-2 epochs. The
105 coloured triangles in Fig. 1f show the magnitude and direction of change in driving stress at
106 ICESat and Envisat cross-over track locations. Maximum changes are about 6 kPa and likely too
107 small to explain the change in the spatial pattern of dh/dt. A recent numerical modelling study
108 infers that both loss of basal traction and surface geometry play a role in modulating mass loss [13].

109 The lower amplitude of thinning in the main trunk could, in part, be due to a weakening in the
110 ocean forcing and, consequently, sub-shelf melting between 2010 and 2012 [7] as reported
111 elsewhere [25]. We note, however, that sub-shelf melt rates increased from 2013 to values similar
112 to those from 1998-2010 (Fig. 4). Our results do not follow the linearly increasing elevation rate
113 proposed for the hinge-line from InSAR and altimetry up to 2010 [26]. Instead, thinning rates have
114 declined by about a factor 6 since their peak in 2009 (Fig. 1e and Extended Fig 2).

Our results indicate a more complex pattern of thinning than previously reported [14] or modelled [9] that is evolving in time (Fig. 2 and Extended Fig 2). Most striking, is the fact that the maximum thinning rates during the CryoSat-2 epoch, exceeding 3 m/yr (Fig. 1g and 2a), are occurring, not in the fast flowing main trunk or tributaries, as previously reported, but beyond the shear margins, in areas of relatively slow-flow (50-100 m/yr) where motion is controlled by ice deformation, not basal sliding. In contrast, the fast-flowing main trunk has mean thinning rates of about a factor three lower than the inter-stream region (Fig. 2a). The peak thinning rate in the inter-stream region is also associated with an acceleration in flow (Fig 1c and f) and a modest increase in gravitational driving stress (Fig. 1f). Thus, mass loss is now propagating into areas of slow, deformation-dominated flow (Fig. 1b). The evolution of thinning (and hence mass loss) for two approximately four-year epochs is shown in Fig 2a and b. Although the central trunk has sped up by about 0.7% during this time (Fig 3b), thinning rates have decreased slightly from the grounding line to about 50 km inland (Fig 2, 3c and Extended Fig 2). The 50% reduction in sub-shelf melting between 2010 and 2012 coincides with a hiatus in ice shelf thinning, as would be expected, which persists until 2013 (Fig. 4)[27]. However, from 2013 ice shelf thinning recommences with a rate comparable to the early 2000s (Fig. 4). We detect a modest increase in the thinning rate close to the grounding line coincident with the resumption of oceanic melting (Fig. 2, 3c and 4) but, in general, the highest thinning rates have shown a decline between 2012 and 2017 (Extended Fig. 2).

Implications for future evolution of PIG

Based on extrapolation of observed thinning rates, it has been suggested that ungrounding of the entire main trunk of PIG within a century was possible[5]. Some model projections for PIG under different ice shelf melt scenarios suggest a 6-fold increase in mass loss and a 40 km migration of

the grounding line in less than two decades [9]. These simulations use an idealised melt scenario and propagate thinning in the central trunk and tributaries, as implied by the satellite radar altimeter observations that were used for comparison [9]. This is, however, not reflected in the present-day evolution of thinning nor the recent behaviour of the glacier. Hence, we investigate what is required to achieve the modelled magnitudes of retreat based purely on geometric constraints and compare with the observations from CryoSat-2. In Fig. 2b we plot the grounding line positions for thinning rates of 2, 5 and 10 m/yr over 50 years alongside the mean rate from CryoSat-2 over the period 2010-2018. The present-day thinning rates result in a negligible grounding line retreat over the next five decades (dashed white line in Fig. 2b). This is consistent with model simulations that suggest modest changes in mass balance and grounding line as a consequence of enhanced sub-shelf melt [6,8]. Even for a mean thinning rate of 5 m/yr (about five times present day), over the central trunk, the grounding line has receded by less than 20 km in 50 years (Fig 2b). We conclude, therefore, in the absence of anomalously high sub-shelf ocean melting, grounding line retreat and accelerated mass loss of PIG will be limited and at the lower end of model estimates leading to about 3 mm sea level equivalent above the present-day imbalance (of ~0.4 mm/yr) over the next five decades[6]. We note, however, that sub-shelf melt rates are sensitive to decadal ocean variability [27,28], have a complex relationship with climate variability[29,30], the geometry of the cavity [31] and tidal pumping close to the grounding line[32].

Implications for vertical land motion from GPS

Our results are also important for the interpretation of vertical land motion, derived from GPS data. These data have been used to constrain geophysical models, and inverse solutions for glacial isostatic adjustment in the Amundsen Sea Embayment [33-36] and to estimate the visco-elastic properties of the mantle at depth[37]. A low mantle viscosity, as inferred for the Amundsen

Sea Embayment, provides a stabilising influence on grounding line migration [37] and is important, therefore, to account for in model projections [38].

The solid Earth deforms rapidly (elastically) to present-day changes in mass loading and slowly (viscously) to past changes. GPS data measure both components and to infer properties of the mantle, and model the viscous response, from GPS data, it is necessary to remove the elastic component due to present-day mass change. This correction is sensitive to the precise spatial distribution of the ice loading changes. It is necessary, therefore, to have detailed knowledge of the spatial pattern of dh/dt at scales of a few kilometres to estimate an accurate elastic correction [37]. [37].. The two GPS stations in Antarctica (INMN and TOMO) with the largest vertical land motion and largest residual, after accounting for glacial isostatic adjustment and elastic deformation, are both close to regions of localised high thinning in the Amundsen Sea Embayment. In the case of INMN (location marked by a star in figure 2), the station lies roughly equidistant between the area of peak thinning rates on the northern flank of PIG and a region further north at about 74.7° S, 99° W. Not only is the amplitude of thinning rapidly evolving during the period of the GPS observations (Extended Fig. 3) but also its spatial pattern. Not accounting for this variability will lead to erroneous estimates of the elastic component of vertical land motion, and, as a consequence, estimates of the visco-elastic properties of the lower mantle [37].

Data availability

The gridded swath processed CryoSat data sets are available from the University of Bristol data portal at https://doi.org/10.5523/bris.xzwd95jqfpok2hi0tkxs5r6at. CryoSat-2 data were provided by the European Space Agency and are available from https://earth.esa.int/web/guest/-/how-to-access-cryosat-data-6842. ICESat-1 data, MEaSURES grounding lines and GoLIVE velocities

184 are available from the National Snow and Ice Data Center, Boulder, Colorado, USA. Envisat
185 data used in this study is available from https://doi.org/10.5270/EN1-ajb696a. The EIGEN-6C4
186 are available from (46), RACMO2.3 from
187 https://www.projects.science.uu.nl/iceclimate/models/antarctica.php and Bedmap2 bedrock
188 topography from https://www.bas.ac.uk/project/bedmap-2/..

189 **References**

190 1 Rignot, E. *et al.* Four decades of Antarctic Ice Sheet mass balance from 1979–2017.
191 *Proceedings of the National Academy of Sciences* **116**, 1095-1103, (2019).
192 2 Hughes, T. West Antarctic Ice Sheet - Instability, Disintegration, and Initiation of Ice
193 Ages. *Rev. Geophys.* **13**, 502-526 (1975).
194 3 Mouginot, J., Rignot, E. & Scheuchl, B. Sustained increase in ice discharge from the
195 Amundsen Sea Embayment, West Antarctica, from 1973 to 2013. *Geophys. Res. Lett.*,
196 **41**, 1576-1584 , (2014).
197 4 Rignot, E. J. Fast recession of a West Antarctic glacier. *Science* **281**, 549-551 (1998).
198 5 Wingham, D. J., Wallis, D. W. & Shepherd, A. Spatial and temporal evolution of Pine
199 Island Glacier thinning, 1995–2006. *Geophys. Res. Lett.* **36**, L17501, (2009).
200 6 Joughin, I., Smith, B. E. & Holland, D. M. Sensitivity of 21st century sea level to ocean-
201 induced thinning of Pine Island Glacier, Antarctica. *Geophys. Res. Lett.* **37**, L20502,
202 (2010).
203 7 Dutrieux, P. *et al.* Strong Sensitivity of Pine Island Ice-Shelf Melting to Climatic
204 Variability. *Science* **343**, 174-178, (2014).
205 8 Seroussi, H. *et al.* Sensitivity of the dynamics of Pine Island Glacier, West Antarctica, to
206 climate forcing for the next 50 years. *Cryosphere* **8**, 1699-1710, (2014).

9 Favier, L. *et al.* Retreat of Pine Island Glacier controlled by marine ice-sheet instability. *Nat. Clim. Chang.* **4**, 117-121, (2014).

10 Jenkins, A. *et al.* Observations beneath Pine Island Glacier in West Antarctica and implications for its retreat. *Nature Geoscience* **3**, 468-472, (2010).

11 Johnson, J. S. *et al.* Rapid Thinning of Pine Island Glacier in the Early Holocene. *Science* **343**, 999-1001, (2014).

12 Vaughan, D. G. *et al.* New boundary conditions for the West Antarctic Ice sheet: Subglacial topography beneath Pine Island Glacier. *Geophys. Res. Lett.* **33**, L09501 (2006).

13 Joughin, I., Smith, B. E. & Schoof, C. G. Regularized Coulomb Friction Laws for Ice Sheet Sliding: Application to Pine Island Glacier, Antarctica. **46**, 4764-4771, (2019).

14 Konrad, H. *et al.* Uneven onset and pace of ice-dynamical imbalance in the Amundsen Sea Embayment, West Antarctica. *Geophys. Res. Lett.* **44**, 910-918, (2017).

15 Wouters, B. *et al.* Dynamic thinning of glaciers on the Southern Antarctic Peninsula. *Science* **348**, 899-903, (2015).

16 Payne, A. J., Vieli, A., Shepherd, A. P., Wingham, D. J. & Rignot, E. Recent dramatic thinning of largest West Antarctic ice stream triggered by oceans. *Geophys. Res. Lett.* **31,** L23401, (2004).

17 Bamber, J. L. & Gomez-Dans, J. L. The accuracy of digital elevation models of the Antarctic continent. *Earth and Planetary Science Letters* **217**, 516-523 (2005).

18 Wingham, D. J. *et al.* in *Natural Hazards and Oceanographic Processes from Satellite Data*, **37** *Advances in Space Research-Series* (eds R. P. Singh & M. A. Shea) 841-871 (2006).

19 Gray, L. *et al.* Interferometric swath processing of Cryosat data for glacial ice topography. *The Cryosphere* **7**, 1857-1867, (2013).

20 Foresta, L. *et al.* Heterogeneous and rapid ice loss over the Patagonian Ice Fields revealed by CryoSat-2 swath radar altimetry. *Remote Sensing of Environment* **211**, 441-455, (2018).

21 Felikson, D. *et al.* Comparison of Elevation Change Detection Methods From ICESat Altimetry Over the Greenland Ice Sheet. *IEEE Trans. Geosci. Remote Sensing* **55**, 5494-5505, (2017).

22 Mouginot, J., Rignot, E., Scheuchl, B. & Millan, R. Comprehensive Annual Ice Sheet Velocity Mapping Using Landsat-8, Sentinel-1, and RADARSAT-2 Data. *Remote Sens.* **9**, 364, (2017).

23 Fahnestock, M. *et al.* Rapid large-area mapping of ice flow using Landsat 8. *Remote Sensing of Environment* **185**, 84-94, (2016).

24 Christianson, K. *et al.* Sensitivity of Pine Island Glacier to observed ocean forcing. *Geophys. Res. Lett.* **43**, 10,817-810,825, (2016).

25 Konrad, H. *et al.* Net retreat of Antarctic glacier grounding lines. *Nature Geoscience* **11**, 258-262 (2018).

26 Park, J. W. *et al.* Sustained retreat of the Pine Island Glacier. *Geophys. Res. Lett.*, **40**, 2137-2142 (2013).

27 Paolo, F. S. *et al.* Response of Pacific-sector Antarctic ice shelves to the El Nino/Southern Oscillation. *Nature Geoscience* **11**, 121-126, (2018).

28 Jenkins, A. *et al.* West Antarctic Ice Sheet retreat in the Amundsen Sea driven by decadal oceanic variability. *Nature Geoscience* **11**, , 733-738 (2018).

29 Davis, P. E. D. *et al.* Variability in Basal Melting Beneath Pine Island Ice Shelf on Weekly to Monthly Timescales. *J. Geophys. Res.-Oceans* **123**, 8655-8669, (2018).

30 Donat-Magnin, M. *et al.* Ice-Shelf Melt Response to Changing Winds and Glacier Dynamics in the Amundsen Sea Sector, Antarctica. *J. Geophys. Res.-Oceans* **122**, 10206-10224, (2017).

31 Schodlok, M. P., Menemenlis, D., Rignot, E. & Studinger, M. Sensitivity of the ice-shelf/ocean system to the sub-ice-shelf cavity shape measured by NASA IceBridge in Pine Island Glacier, West Antarctica. *Annals of Glaciology* **53**, 156-162, (2012).

32 Milillo, P. *et al.* On the Short-term Grounding Zone Dynamics of Pine Island Glacier, West Antarctica, Observed With COSMO-SkyMed Interferometric Data. *Geophys. Res. Lett.* **44**, 10,436-10,444 (2017).

33 Argus, D. F., Peltier, W. R., Drummond, R. & Moore, A. W. The Antarctica component of postglacial rebound model ICE-6G_C (VM5a) based on GPS positioning, exposure age dating of ice thicknesses, and relative sea level histories. *Geophysical Journal International* **198**, 537-563, (2014).

34 Gunter, B. C. *et al.* Empirical estimation of present-day Antarctic glacial isostatic adjustment and ice mass change. *Cryosphere* **8**, 743-760, (2014).

35 Ivins, E. R. *et al.* Antarctic contribution to sea level rise observed by GRACE with improved GIA correction. *J. Geophys. Res.*, **118**, 3126-3141 (2013).

36 Martín-Español, A. *et al.* An assessment of forward and inverse GIA solutions for Antarctica. *J. Geophys. Res.*, **121**, 6947– 6965 (2016).

37 Barletta, V. R. *et al.* Observed rapid bedrock uplift in Amundsen Sea Embayment promotes ice-sheet stability. *Science* **360**, 1335-1339, Science (2018).

38 Larour, E. *et al.* Slowdown in Antarctic mass loss from solid Earth and sea-level feedbacks. *Science* **364**, eaav7908, (2019).

39 Helm, V., Humbert, A. & Miller, H. Elevation and elevation change of Greenland and Antarctica derived from CryoSat-2. *Cryosphere* **8**, 1539-1559, (2014).

40 Padman, L., Fricker, H. A., Coleman, R., Howard, S. & Erofeeva, L. *Ann. Glaciol.*, **34** 247-254 (2002).

41 Fretwell, P. *et al.* Bedmap2: improved ice bed, surface and thickness datasets for Antarctica. *Cryosphere* **7**, 375-393, (2013).

42 Gray, L. *et al.* A revised calibration of the interferometric mode of the CryoSat-2 radar altimeter improves ice height and height change measurements in western Greenland. *Cryosphere* **11**, 1041-1058, (2017).

43 Borsa, A. A., Moholdt, G., Fricker, H. A. & Brunt, K. M. A range correction for ICESat and its potential impact on ice-sheet mass balance studies. *Cryosphere* **8**, 345-357, (2014).

Acknowledgments: We thank G.H. Gudmundsson and I. Joughin for comments on a draft of the manuscript. We would also like to thank two anonymous referees for their constructive and thoughtful comments that considerably improved the manuscript. This work was supported by the UK Natural Environment Research Council (NERC) grant NE/N011511/1. JLB was also supported by the European Research Council under grant agreement 694188 and a Royal Society Wolfson Merit Award.

Author contributions JLB conceived the study and wrote the paper, GD undertook the data analysis and developed the methods. Both authors commented on the manuscript. The authors declare no competing interests.

Ethics declarations

Competing interests

The authors declare no competing interests.

Figure 1. PIG elevation, velocity and driving stress changes between 2005 and 2018.

a) Elevation and bedrock topography (Bedmap2) profiles for ICESat-1 track 279 across PIG. b) elevation and c) across-track and d) along-track velocity change for the period between 2005 to 2009 (black) and 2010 to 2017 (red). (e) Mean elevation change calculated using ICESat-1 between 2005 to 2009 (black) and CryoSat-2 between 2010-2018 (red). (f) map of ice velocity change for the period between 2005-2009 and 2010-2017 (with white directional arrows) near the grounding line. The average change in driving stress (τ) at ICESat-1/ Envisat crossover points is also shown in (f) with coloured directional arrows. The change in driving stress was calculated between the periods 2005-2009 and 2010-2018 using ICESat-1and CryoSat-2 (solid outline) and between the periods 2002-2010 and 2010-2018 using Envisat and CryoSat-2 (double-line outline). The mean surface elevation rate calculated from ICESat-1 data, overlain on the mean elevation rate derived from CryoSat-2 swath data at 500 m posting (g). The dotted black line is the grounding line position recorded before 2003,the solid black line is the position recorded in 2011 and the solid green (f) or grey (g) lines are the positions recorded in 2015 [32]. Contours are mean velocities for the period 2005-2017.

Figure 2. Elevation change over PIG between 2010 and 2018.

Mean surface elevation rate derived from CryoSat-2 swath data between a) 2010-2014 and b) 2015-2018, gridded at 2km postings with no smoothing. The dark red lines in a) are mean velocity contours for the period 2005-2017 and in b) are 100 m, 250 m and 500 m contours of height above flotation using the assumption of hydrostatic equilibrium (i.e. floatation point after 50 years for a thinning rate of 2m/y, 5 m/y and 10 m/y respectively). The dashed white line is the

floatation point after 50 years using the mean CryoSat-2 thinning rates, and the black line is a composite of the 2011 and 2015 grounding line position. The star is the location of the INMN GPS station. The thick solid black line running east to west is the flow line path for the cross-section used in Fig. 3 and the dashed black box is the area shown in Fig. 1.

Figure 3. Profile along a central flowline of PIG.

a) Elevation and bedrock topography (Bedmap2), the blue line is the predicted ice sheet elevation needed for flotation. The vertical blue dashed lines are the intersections with the 100 m, 250 m and 500 m contours of height above flotation in Fig. 2. The vertical black dashed lines are the grounding line positions recorded in 1) 2003 and 2) in 2011. b) Ice velocity change recorded calculated between 2013 and 2017 and c) mean surface elevation rate for CryoSat-2 between 2010-2014 (black) and 2015-2018 (red)..

Figure 4. Ice shelf thinning rates for PIG, 1994-2017.

Pine Island Glacier ice shelf height change derived using ERS-1 (1991–1996), ERS-2 (1995–2003), Envisat (2002–2012) and CryoSat-2 (2010–2017) from Paolo *et al.* 2018 [27]. The black line is the original time series, which has a 3 month time step. The red line is the data smoothed with a 4 year moving-window filter.

Methods

CryoSat-2 Elevation

We used CryoSat-2 synthetic aperture radar interferometric (SARIn) L1b baseline C data spanning between October 2010 (referred in the text as 2010) and December 2018 in this study. With these data we were able to use the necessary corrections, position/timing information along with the waveform power, coherence and phase to calculate Point Of Closest Approach (POCA) and "swath processed" heights, which are derived from the time-delayed waveform beyond the first return. The processing scheme used here closely follows Gray *et al*. (2013) [19]. The processing first involved using a threshold re-tracker described in Helm et al 2014[39] to determine the POCA, and selecting swath samples with a minimum coherence and power of 0.8 and -150 dB, respectively. We then calculated the range for the POCA and each swath sample, corrected for path delay due to the wet and dry troposphere and ionosphere, and changes in surface height for the solid earth and ocean loading tides. Over the ice shelves, we also corrected for inverse barometric atmospheric pressure and tidal variability using the CAT2008a tide model, which is an update to the model described in Padman *et al.* [40]. Phase wrapping and ambiguity errors can occur in areas of high sloping terrain, and these were corrected by unwrapping the phase around a reference phase difference. The reference phase difference was created by sampling the Bedmap2 Digital Elevation Model [41] in the cross-track direction for a range of cross-track look-angles through the antenna beam half width (1.992°). This was then re-sampled to the sample points and the look-angle (θ) was converted to phase (ψ) using

$$\sin(\theta + \beta) = -\psi/kB \quad (1)$$

where B is interferometric baseline, β is roll angle and k is wavenumber [19]. We then applied a multiple of 2π correction to match the measured phase to the reference phase. This method is reliable in areas of complex topography as it can successfully unwrap data with multiple phase discontinuities. The satellite orientation and the phase information was then used to calculate cross-track look-angles using equation (1) and was combined with the range to calculate the elevation and location of the return echo relative to the reference ellipsoid.

CryoSat-2 elevation rates

We calculated a linear surface elevation rate (dh/dt) with CryoSat-2 data on a grid of 4 km posting for POCA data, and between 0.5 km and 4 km postings for swath data using

$$h = a_o + a_1 x + a_2 y + \frac{dh}{dt} t \quad (2)$$

where h is elevation, a_o is mean elevation and t is time. To account for variation in topography within each grid cell, we simultaneously solved for surface slopes a_1 and a_2, in the x and y direction, respectively. The noise observed within swath data, typically has standard deviations between ~1 m and ~3 m [42], and can also include large outliers (e.g. incorrectly geolocated return echoes) which could adversely affect the fitting process. To account for these, we used a robust method by iteratively re-weighing the least squared regression with a bi-square weighting (w) of the form $w = (1 - (r/7m)^2)^2$ where r is the residuals of the previous fit and m is the median absolute deviation.

In the fast-flowing areas, the elevation change will be affected by advecting ice. This is particularly apparent over floating ice and can be removed using a Lagrangian framework [43]. However, such a framework is only valid over ice in hydrostatic equilibrium, and as our study

focused on the grounded portion of the ice shelf, this was not performed, and the resulting fast-flowing areas still contain this noise. We calculated the surface elevation rate over the entire CryoSat-2 recorded from 2010-2018. We also calculated a linear elevation rate for two separate periods between 2010-2014 and 2015-2018 and for a three-year moving window weighted using a tri-cube function. For the two separate periods between 2010-2014 and 2015-2018, the increase in temporal resolution required us to use a grid of 2 km posting, while for the three-year moving window we used a grid of 4 km posting. We incorporated POCA data into the three-year moving window calculation by using the mean value between POCA and swath data.

The standard error of the model fit was used to estimate the uncertainty in elevation rates (Extended Fig. 3). This measure includes any departure from the model and any measurement error, for example, from incorrectly modelled atmospheric corrections, uncertainty in the location of the measurement either from the orbit location or the geolocation of the radar echo. Errors from incorrect geolocation of the return, arising from ambiguous reflections over complex/steep topography may introduce a variable bias, and the standard error to the model fit will not adequately capture this. However, the choice of a relatively high coherence threshold ensures that the majority of these data have been removed from our analysis. Over the entire study area, the average standard error was 0.2 m/y. While over the fast-moving areas, elevation measurements were affected by ice advection and the standard error was higher. In these regions where dv/dt>1000 m/y, the average uncertainty is 0.4 m/y.

ICESat-1 elevation rates

ICESat-1 laser altimeter elevation data (GLAS/ICESat L2 Global Land Surface Altimetry Data, version 34, GLA14) were pre-processed using the data pre-processing steps described in

Felikson *et al*. (2017) [21]. Elevation rates were then calculated using the repeat-track method by first binning elevation data from all campaigns into non-overlapping grid cells of 1 km by 1 km along a reference track. Elevation change was then determined using

$$h = a_o + a_1 x + a_2 y + \frac{dh}{dt} t \quad (3)$$

where is the a_1 and a_2 are the slopes of the topography in the x and y direction [21]. The elevation change was measured over the ICESat-1 operation period which was between February 2003 and October 2009. The uncertainty in elevation rates were measured using the standard error of the model fit (Extended Fig. 3). Over the entire study area, the standard error was 0.1 m/y, while over the fast-moving central section of Pine Island Glacier (dv/dt>1000 m/y), the standard error was 0.2m/y.

Ice velocity and grounding line location

Ice velocity change over Pine Island Glacier was determined using two datasets described in Supplementary Table 1. We first used data from MEaSUREs Version 1 [22,44], as this had a sufficient time span to cover both ICESat-1 and CryoSat-2 satellite epochs. The ice velocity change for these data was found by calculating the average x and y components of the ice velocity within the separate time periods 2005-2009 and 2011-2017 within each 1 km grid cell, then calculating the difference. We also used the GoLIVE velocity time series [23,45] to measure ice velocity change within the CryoSat-2 period. GoLIVE has a higher spatial and temporal resolution of 300 m and 16 days, respectively. This allowed us to calculate a linear trend for the x and y components of the velocity, which we measured over a grid of 1 km posting. Acceleration over Pine Island Glacier is shown in Extended Fig. 4.

We used the grounding line positions from MEaSUREs version 2 in this study [44]. This dataset used differential satellite radar interferometry to determine the hinge-line. Over Pine Island Glacier, grounding line position was measured primarily using the ERS satellites and was recorded several times before 2003, in 2011 and 2015 [32].

Driving stress

The driving stress (τ) was calculated using a force balance approach with the assumption of small surface slope (α)

$$\tau = \rho_I g Z \alpha \quad (4)$$

where ρ_I is the density of ice, taken as 917 kg/m^3 and Z the ice thickness. The driving stress for the ICESat-1 data was calculated by first determining the driving stress in the along-track direction for both ascending (τ_a) and descending (τ_d) tracks. We used the elevation measurements at the mid-point of the ICESat-1 operation period (i.e. September 2006) derived from the repeat-track method used in Section 1.3. A 10 km gaussian filter was applied before determining the surface slope, as this provided a representation of the driving stress for the scale of the ice thickness. We then calculated the driving stress in the x (τ_x) and y (τ_y) directions by determining the driving stress at crossover points. This is similar to the method described by Sandwell and Smith (1997) [46] who used the vertical deflections at the satellite crossover point, to calculate marine gravity with radar altimeters. Using this methodology, we first defined the driving stress of an ascending track as

$$\tau_a = \tau_x \dot{x}_a + \tau_y \dot{y}_a \quad (5)$$

and for a descending track

462 $$\tau_d = \tau_x \dot{x}_d + \tau_y \dot{y}_d \quad (6)$$

463 where $\dot{x}$ and $\dot{y}$ are the x and y components of the satellite track. Then at each crossover point, we
464 simultaneously solved equations (5) and (6) to determine τ_x and τ_y. The optimal situation is
465 when the tracks intersect perpendicular to one another, however the ICESat-1 ascending and
466 descending tracks in this region intersect at an angle of ~33°. This results in the driving stress
467 being poorly resolved in the y direction for this area of study (using the polar stereographic
468 projection system, EPSG:3031). We calculated driving stress for CryoSat-2 using the same
469 method and elevation measurement at the mid-point of the study period (i.e. February 2014),
470 which were sampled onto the ICESat-1 tracks. We could also calculate the driving stress for
471 CryoSat-2 on a grid, which would enable us to fully resolve the driving stress. However, this
472 would not allow for a direct comparison with ICESat-1.

473 To improve coverage, we also used Envisat radar altimetry data to calculate the change in
474 driving stress between Envisat and CryoSat-2 using the same method described above. The
475 Envisat elevation data were processed using the along-track processing described in Flament and
476 Remy, 2012 [47] and spanned between January 2003 and November 2010. The mean elevation
477 over that time period was used for this comparison.

478

479 **Height above floatation**
480
481 To calculate the height above floatation (h_f), we combined CryoSat-2 swath elevations, bedrock
482 topography from Bedmap2 [41] and the EIGEN-6C4 geoid [48] to deduce ice thickness (Z) and
483 elevation above mean sea level (h), using the assumption of hydrostatic equilibrium

$$h_f = h - \frac{(Z-\delta)(\rho_w - \rho_I)}{\rho_W} - \delta$$

where δ is the air content of the firn layer obtained from a regional climate model, RACMO2.3[49] expressed in meters of ice equivalent. The densities of 1027 kg/m^3 and 917 kg/m^3 were used for sea water (ρ_I) and ice (ρ_w) respectively.

44 Rignot, E., Mouginot, J. & Scheuchl, B. (ed National Snow and Ice Data Center Distributed Active Archive Center) (National Snow and Ice Data Center Distributed Active Archive Center, Boulder, Colorado, USA, 2016).

45 Scambos, T., Fahnestock, M., Moon, T., Gardner, A. & Klinger, M. (ed National Snow and Ice Data Center Distributed Active Archive Center) (National Snow and Ice Data Center Distributed Active Archive Center, 2016).

46 Sandwell, D. T. & Smith, W. H. F. Marine gravity anomaly from Geosat and ERS 1 satellite altimetry. *J. Geophys. Res.* **102**, 10039-10054, (1997).

47 Flament, T. & Remy, F. in *2012 IEEE International Geoscience and Remote Sensing Symposium IGARSS* 1848-1851 (2012).

48 Förste, C. et al. EIGEN-6C4 The latest combined global gravity field model including GOCE data up to degree and order 2190 of GFZ Potsdam and GRGS Toulouse (2014).

49 Van Wessem, J. et al. Improved representation of East Antarctic surface mass balance in a regional atmospheric climate model. *J. Glaciol.*, **60**, 761-770 (2014)

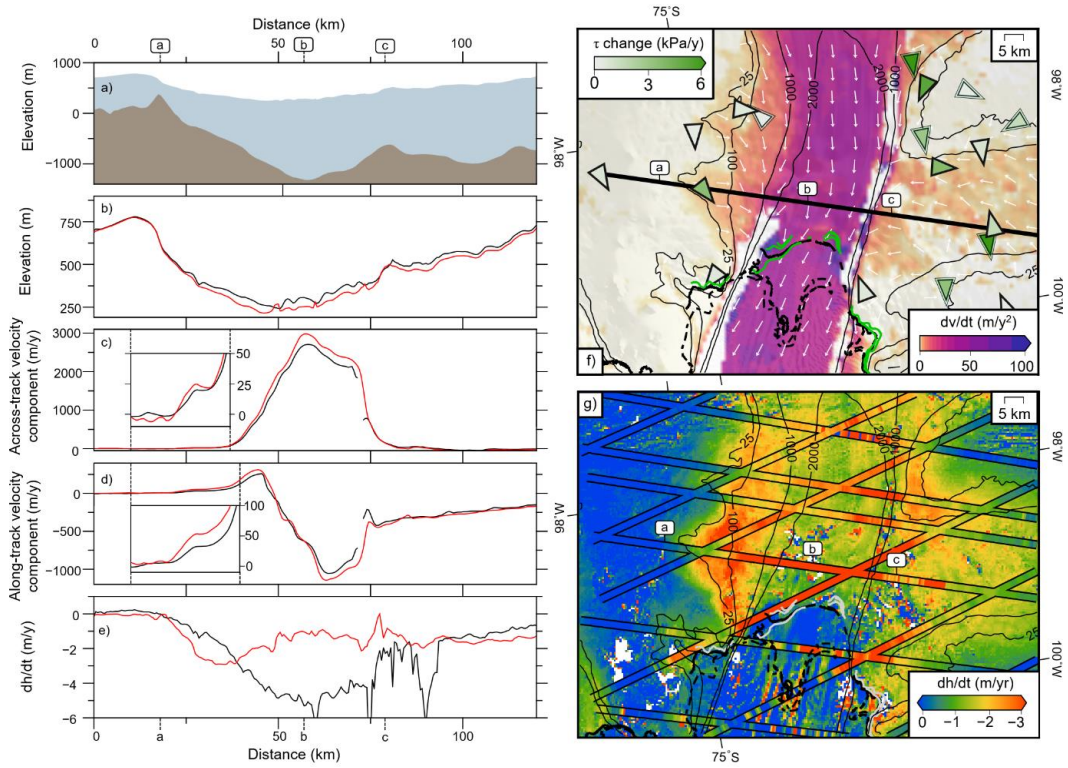

502

503 Fig 1

504

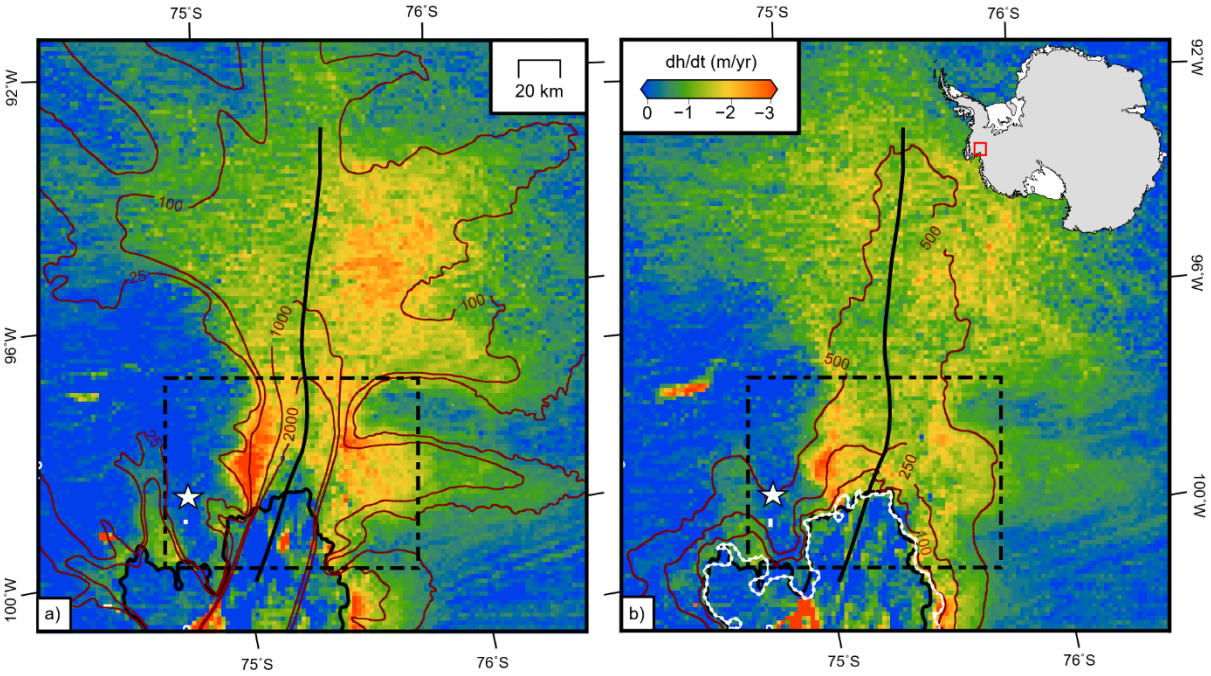

505

506 Fig 2

507

508

509

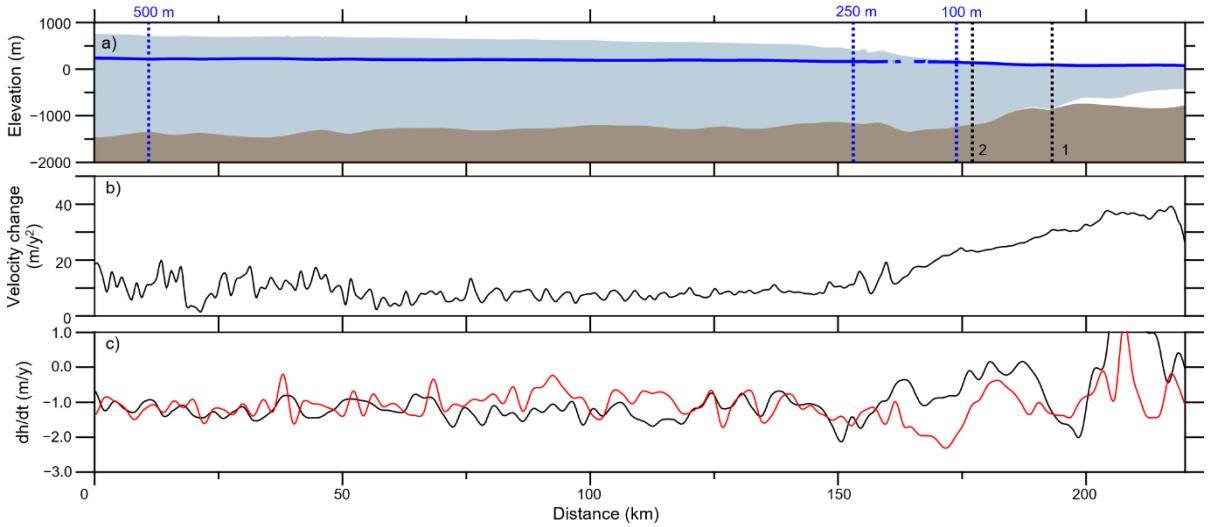

510

511 Fig 3

512

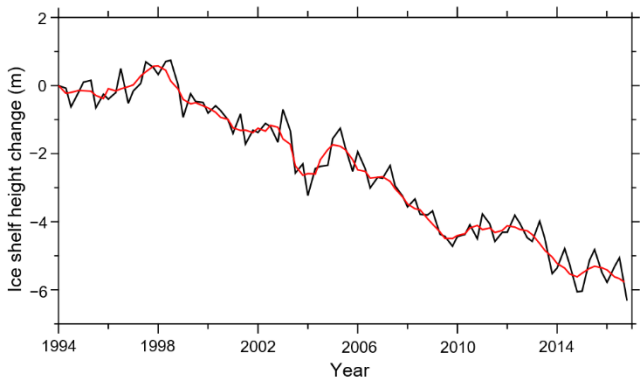

513

514 Fig 4

515

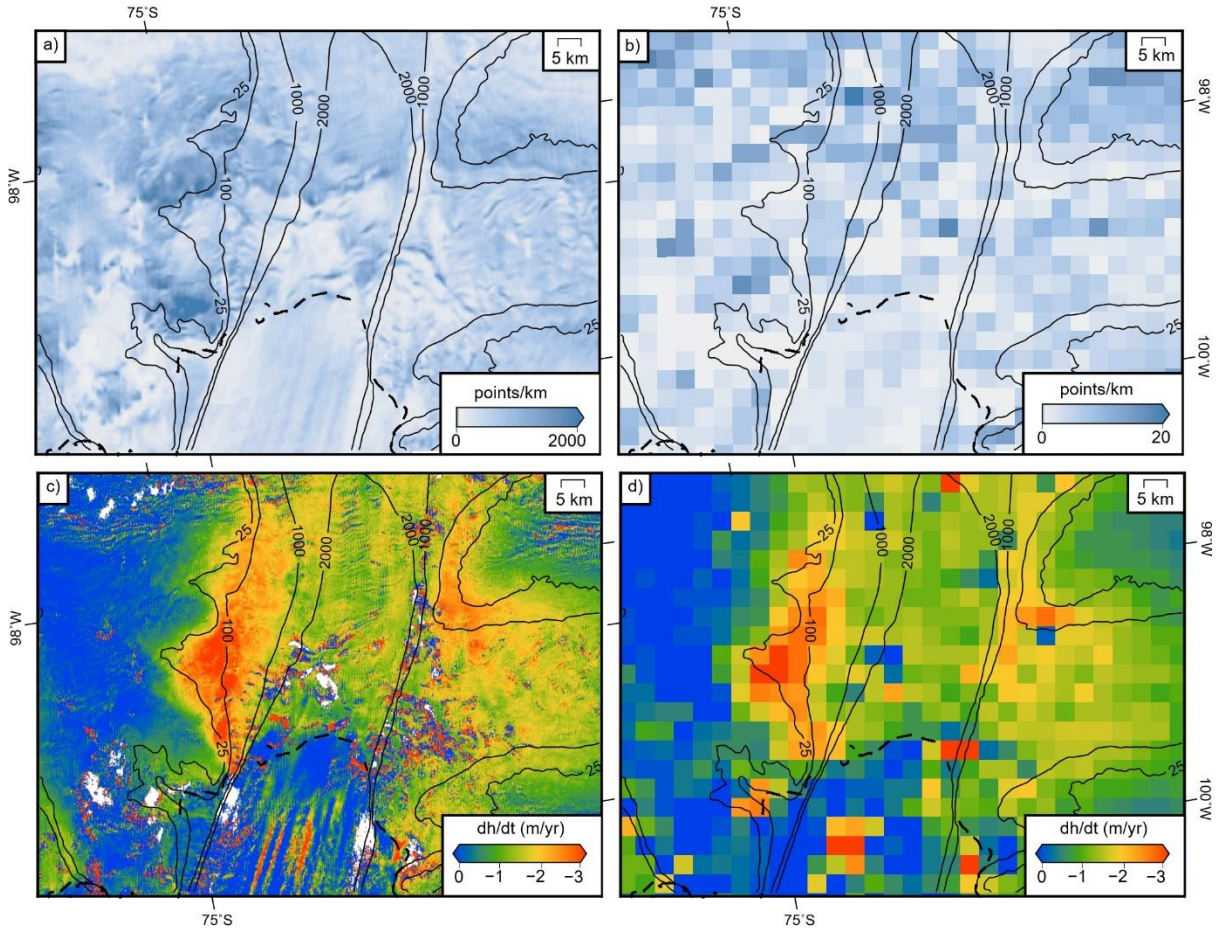

516

517 Extended Fig 1

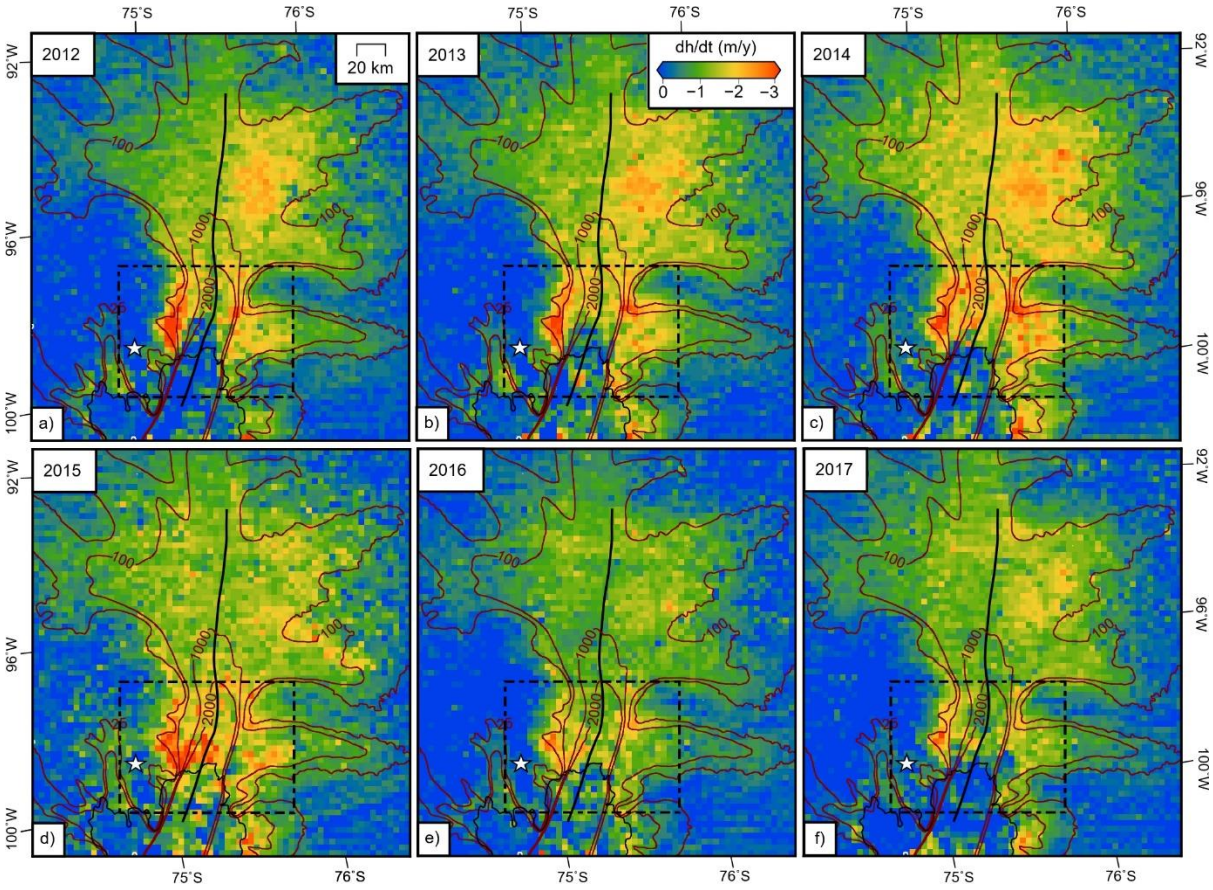

Extended Fig 2

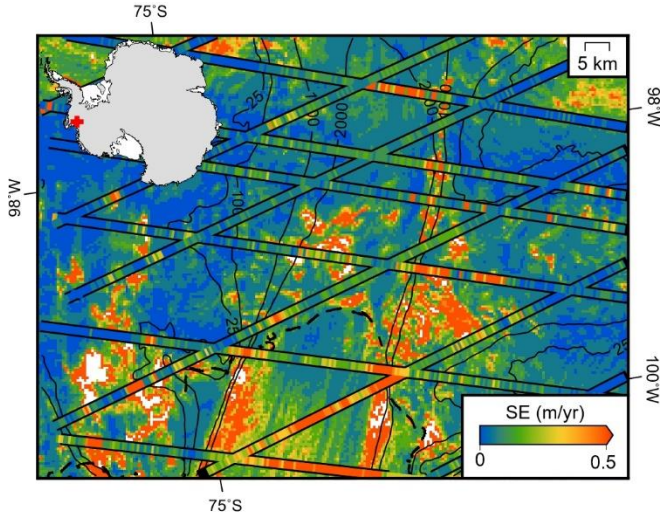

521

522 Extended Fig 3

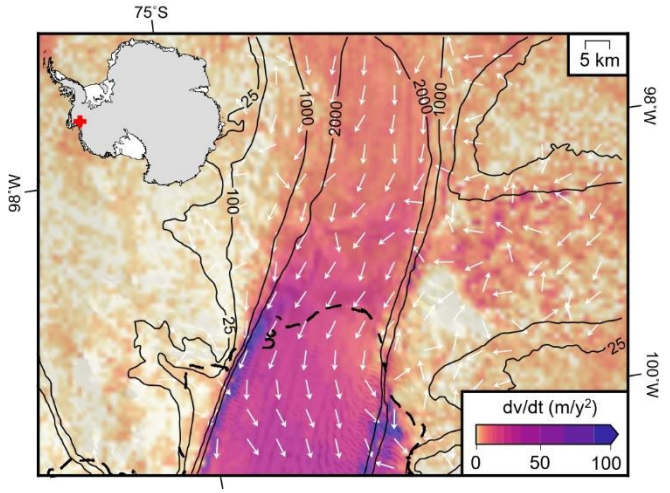

523

524 Extended Fig 4.

525